Response of land surface fluxes and precipitation to different soil bottom hydrological conditions in a general circulation model

A. Campoy, Agnès Ducharne, F. Cheruy, F. Hourdin, J. Polcher, J.C. Dupont

Response of land surface fluxes and precipitation to different soil bottom hydrological conditions in a general circulation model

A. Campoy,[1] A. Ducharne,[1] F. Cheruy,[2] F. Hourdin,[2] J. Polcher,[2] and J. C. Dupont[3]

Received 9 January 2013; revised 1 July 2013; accepted 4 July 2013; published 2 October 2013.

[1] Very different approaches exist in land surface models (LSMs) to describe the water fluxes at the soil bottom, from free drainage to zero flux, and even upward fluxes if the soil is coupled to a water table. To explore the influence of these conditions on the water cycle in a unified framework, we introduce new boundary conditions in the ORCHIDEE LSM, which is coupled to the atmospheric general circulation model LMDZ. We use a zoomed and nudged configuration centered over France to reproduce the observed regional weather. Soil moisture and evapotranspiration increase ranging from free drainage to impermeable bottom, then by prescribing saturation closer and closer to the surface. The corresponding response patterns can be related to both climate regimes and soil texture. When confronted to observations from the SIRTA observatory 25 km south of Paris, which exhibits a shallow water table, the best simulations are the ones with prescribed saturation. The local precipitation, however, is only increased if the new bottom boundary conditions are applied globally. The magnitude of this increase depends on the evaporation and on the relative weight of local versus remote sources of moisture for precipitation between Western and Eastern Europe. This suggests that the summer warm/dry bias of many climate models in this region might be alleviated by including a sufficiently realistic ground water description.

Citation: Campoy, A., A. Ducharne, F. Cheruy, F. Hourdin, J. Polcher, and J. C. Dupont (2013), Response of land surface fluxes and precipitation to different soil bottom hydrological conditions in a general circulation model, *J. Geophys. Res. Atmos.*, *118*, 10,725–10,739, doi:10.1002/jgrd.50627.

1. Introduction

[2] Soil hydrology is a key component of land surface models (LSMs), as it interacts with vegetation functioning and dynamics, water resources (river discharge, groundwater, and irrigation), as well as turbulent fluxes to the atmosphere. When coupled to an atmospheric model, it introduces a surface-atmosphere feedback loop [*Schär et al.*, 1999; *Ducharne and Laval*, 2000; *Koster et al.*, 2004; *Betts*, 2007; *Cheruy et al.*, 2013], with rather long time constants, of typically 1 year [*Entekhabi et al.*, 1996; *Oki et al.*, 2004]. A very active research is thus devoted to understanding the consequences of this "memory" of continental climate in terms of predictability, persistence of extreme events, or anthropogenic climate change trajectory [*Koster and Suarez*, 2001; *Dirmeyer et al.*, 2009; *Seneviratne et al.*, 2010; *Quesada et al.*, 2012].

[3] Yet soils are often linked to a water table; in which case, the latter contributes to the variability of soil moisture. Spatially, this influence is particularly visible at the scale of river catchments, where soil moisture is usually higher in valleys than over hillslopes, because of groundwater convergence to the draining streams. Temporally, water tables are often expected to exert a buffering influence on soil moisture variability and thus to increase the land surface memory, as they can store the wet season water excess and release it progressively during the dry season, which can then sustain higher evaporation rates. This effect, however, depends a lot on water table depth and is particularly strong if the latter is small enough for capillary rise to reach the root zone [*Kollet and Maxwell*, 2008; *Lo and Famiglietti*, 2010; *Gleeson et al.*, 2011a].

[4] As a result, the effects of water tables on the spatial and temporal variability of soil moisture are not independent, which led to incorporate the concepts of TOPMODEL [*Beven and Kirkby*, 1979] in several LSMs to describe the resulting subgrid-scale variability of soil moisture [*Famiglietti and Wood*, 1994; *Stieglitz et al.*, 1997; *Koster et al.*, 2000; *Niu and Yang*, 2003]. Alternatives are to fully couple an LSM with a high-resolution 2-D or 3-D groundwater model, which has only been achieved at regional to continental scales for the time being [*York et al.*, 2002; *Kollet and Maxwell*, 2008; *Anyah et al.*, 2008]. In LSMs, however, the interactions between the soil and the water

[1]UMR 7619 Sisyphe, Université Pierre et Marie Curie/CNRS, Paris, France.
[2]UMR 8539 Laboratoire de Météorologie Dynamique, Université Pierre et Marie Curie/CNRS, Paris, France.
[3]SIRTA, IPSL, Ecole Polytechnique, Palaiseau, France.

Corresponding author: A. Ducharne, UMR 7619 Sisyphe, Université Pierre et Marie Curie/CNRS, Paris, France. (Agnes.Ducharne@upmc.fr)

2169-897X/13/10.1002/jgrd.50627

table are more frequently addressed one-dimensionally, with different modeling frameworks depending on whether saturation is allowed within the simulated soil column [*Liang et al.*, 2003; *Maxwell and Miller*, 2005; *Varado et al.*, 2006; *Zeng and Decker*, 2009] or not [*Yeh and Eltahir*, 2005; *Niu et al.*, 2007; *Lo and Famiglietti*, 2011; *Vergnes and Decharme*, 2012].

[5] These two strategies correspond to different conceptualizations of soil water flow but also to different bottom boundary conditions to the simulated soil column [*Gulden et al.*, 2007]. In the first case, both saturated and unsaturated flow need to be described and the soil column is extended to the water table floor, which is assumed to be impermeable (zero flux). In the second case, the boundary flux at the soil bottom is deduced from hydraulic gradients between the soil bottom and the underlying water table, with possible upward fluxes. These two cases are yet different from the most classical description of soil water flow in LSMs, which assume unsaturated soils and free downward drainage at the soil bottom [e.g., *Abramopoulos et al.*, 1988; *Ducharne et al.*, 1998; *De Rosnay et al.*, 2002; *Decharme et al.*,2011], except in bucket-type models which assume an impermeable bottom, but do not describe water table building [*Manabe*, 1969; *Ducoudré et al.*, 1993].

[6] Despite this diversity of approaches, the role of the soil bottom hydrological conditions is largely overlooked in LSMs, and the aim of this paper is to explore it in a unified framework. We benefit from atmospheric and soil measurements collected at the SIRTA (Site Instrumental de Recherche par Télédétection Atmosphérique) observatory in France [*Haeffelin et al.*, 2005], which revealed the presence of a shallow water table. This site thus offers an interesting case study to assess the pertinence of various soil bottom boundary conditions on (i) the soil moisture and land surface fluxes simulated by the Organizing Carbon and Hydrology in Dynamic Ecosystems (ORCHIDEE) LSM [*Krinner et al.*, 2005], (ii) the regional climate, owing to the coupling of ORCHIDEE with the atmospheric model LMDZ of the Laboratoire de Meteorologie Dynamique [*Hourdin et al.*, 2006].

[7] The ORCHIDEE LSM is first described in section 2, with a focus on the tested soil bottom hydrological conditions. The resulting simulations performed with the coupled model ORCHIDEE-LMDZ, and the evaluation design based on SIRTA's observations, are then presented in section 3. The results follow in section 4, and include a local-scale analysis focused on hydrological and atmospheric processes, a regional-scale analysis focused on the links between the water cycle and the atmospheric circulation, and a discussion of this work's limits. The main conclusions and future research perspectives are finally proposed in section 5.

2. The Land Surface Model ORCHIDEE

2.1. Overview

[8] ORCHIDEE is the LSM of the IPSL (Institut Pierre-Simon Laplace) climate model. The SECHIBA (Schématisation des EChanges Hydriques à l'Interface entre la Biosphère et l'Atmosphère) module describes the water and energy budget of the land surface as a result of interactions between soil, vegetation, and atmosphere within rectangular grid cells. In each of them, the heterogeneous vegetation cover is described by a mosaic of uniform vegetation tiles. Their properties, which includes foliage and root's property, can be selected from 13 plant functional types (PFTs).

[9] As detailed in *Krinner et al.* [2005], ORCHIDEE also includes options to simulate the carbon cycle, using the STOMATE (Saclay Toulouse Orsay Model for the Analysis of Terrestrial Ecosystems) module for photosynthesis and phenology, and the LPJ (Lund-Potsdam-Jena) module for vegetation dynamics (fire, sapling establishment, light competition, tree mortality, and climatic criteria for the introduction or elimination of PFTs). Here, to shut down possible retroactions, these two modules are not activated, and the distribution of the PFTs is prescribed, as detailed in *Verant et al.* [2004].

[10] Two different soil hydrology modules are available in ORCHIDEE. The first one is a simple two-layer bucket-type model [*Ducoudré et al.*, 1993]. The second one, used here, is based on the vertical discretization of a 2 m soil column to calculate the unsaturated water flow using the *Richards* [1931] equation. Transpiration is coupled to the resulting soil moisture profile owing to a root density profile [*De Rosnay and Polcher*, 1998]. Bare soil evaporation is limited by soil moisture availability in the top layer, while the other two terms of evapotranspiration, namely interception loss and snow sublimation, do not depend on soil moisture. In case of precipitation, a time-splitting procedure based on *Green and Ampt* [1911] assumptions is used to partition throughfall between surface runoff and infiltration into the soil, by characterizing the wetting front speed through the top soil layers [*D'Orgeval et al.*, 2008]. Note finally that the 13 PFTs are grouped into three ensembles (bare soil, trees, and grass/crop), defining three independent soil columns with separate water budgets.

2.2. Physical Description of Soil Water Fluxes

[11] *De Rosnay et al.* [2002] introduced a physically based description of unsaturated soil water flow in ORCHIDEE, based on the one-dimensional Fokker-Planck equation. It combines the mass and momentum conservation equations using volumetric water content θ ($m^3\ m^{-3}$) as a state variable, instead of pressure head as in the Richards equation.

[12] Due to the large scale at which ORCHIDEE is usually applied, we neglect the lateral fluxes between adjacent grid cells. We also assume all variables to be horizontally homogeneous, so that the mass conservation equation relating the vertical distribution of θ to its flux field q ($m\ s^{-1}$) is the following:

$$\frac{\partial\theta(z,t)}{\partial t} = -\frac{\partial q(z,t)}{\partial z} - s(z,t). \tag{1}$$

In this equation, z is the depth below the soil surface, and t is the time (in m and s, respectively). The sink term s ($m^3\ m^{-3}\ s^{-1}$) is due to transpiration and depends on the root's density profile.

[13] The flux field q comes from the equation of motion known as *Darcy* [1856] equation in the saturated zone and extended to unsaturated conditions by *Buckingham* [1907]:

$$q(z,t) = -D(\theta(z,t))\frac{\partial\theta(z,t)}{\partial z} + K(\theta(z,t)). \tag{2}$$

$K(\theta)$ and $D(\theta)$ are the hydraulic conductivity and diffusivity (in $m\ s^{-1}$ and $m^2\ s^{-1}$, respectively), given in ORCHIDEE by

Table 1. Hydraulic Parameters for Each Soil Textural Class Defined in ORCHIDEE

Parameter	Unit	Sandy Loam	Medium Loam	Clay Loam
θ_s	$m^3\ m^{-3}$	0.41	0.43	0.41
θ_r	$m^3\ m^{-3}$	0.065	0.078	0.095
K_s	$mm\ d^{-1}$	1060.8	249.6	62.4
α	m^{-1}	7.5	3.6	1.9
m	-	0.471	0.359	0.237

the *Mualem* [1976] and *Van Genuchten* [1980] model:

$$K(\theta) = K_s \sqrt{\theta_f} \left(1 - \left(1 - \theta_f^{1/m}\right)^m\right)^2, \quad (3)$$

$$D(\theta) = \frac{(1-m)K(\theta)}{m\alpha} \frac{1}{\theta - \theta_r} \theta_f^{-1/m} \cdot \left(\theta_f^{-1/m} - 1\right)^{-m}, \quad (4)$$

where K_s is the saturated hydraulic conductivity ($m\ s^{-1}$) and α and m are the parameters. These equations assume that θ varies between the residual water content θ_r and the saturated water content θ_s, which leads to define relative humidity as $\theta_f = (\theta - \theta_r)/(\theta_s - \theta_r)$.

[14] In this framework, ORCHIDEE takes into account the soil's characteristics through parameters K_s, θ_s, θ_r, α, and m, which are defined here for three soil textures. Their geographical distribution is given by the Food and Agriculture Organization map, as interpolated by *Zobler* [1986]. This author's original five textural classes (fine, medium-fine, medium, medium-coarse, and coarse) are reduced to three (fine, medium, and coarse), the medium one comprising the medium-fine, medium, and medium-coarse Zobler classes. The above five hydraulic parameters are then taken from *Carsel and Parrish* [1988] for the corresponding U.S. Department of Agriculture (USDA) soil textural class (Table 1). In addition, following *D'Orgeval et al.* [2008], K_s is assumed to be constant within the top 30 cm but to exponentially decrease further down, as initially introduced by *Beven and Kirkby* [1979]. To keep the consistency between K_s and the parameters α and m, the latter are also modified below 30 cm, based on their log-log regression with K_s, using the values given by *Carsel and Parrish* [1988] for the 12 USDA soil textures.

2.3. Finite Difference Integration

[15] The Fokker-Planck equation, as defined by the combination of equations (1)–(2), is solved using the finite difference method with an implicit scheme. To this end, the 2 m soil column is discretized using N nodes, defined by an index i increasing from top to bottom, and where we calculate the values of θ (Figure 1). The middle of each consecutive couple of nodes represents the limit between two soil layers, except for the upper and the lower layers defined by the first and the last nodes, respectively. As a consequence, each soil layer holds only one node i, and we define layer i as the layer holding node i.

[16] The total water content of each layer i, W_i (m^3), is obtained by integration of $\theta(z)$, assumed to undergo linear variations between two consecutive nodes. Equation (1) can then be integrated between the nodes and over the time step dt, over which q is assumed to be constantly equal to its value at $t + dt$. This allows defining the water budget of each layer i:

$$\frac{W_i(t+dt) - W_i(t)}{dt} = Q_{i-1}(t+dt) - Q_i(t+dt) - S_i, \quad (5)$$

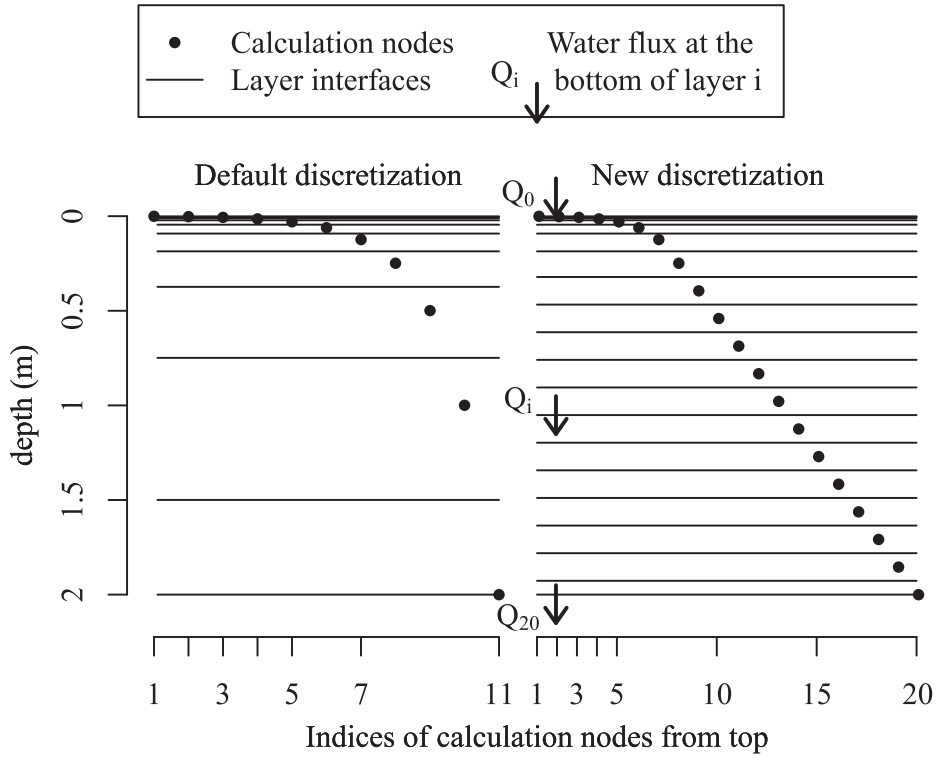

Figure 1. Soil vertical discretization: (left) default 11-layer discretization from *De Rosnay et al.* [2002], (right) new 20-layer discretization.

where S_i is the integrated sink term and Q_i is the water flux at the interface between layers i and $(i + 1)$.

[17] This flux is deduced from equation (5), by approximating $\partial\theta/\partial z$ by the rate of increase between the equidistant neighboring nodes $(i - 1)$ and i, and this leads to:

$$\frac{Q_i}{A} = -\frac{D(\theta_{i-1}) + D(\theta_i)}{2}\,\frac{\theta_i - \theta_{i-1}}{dz_i} + \frac{K(\theta_{i-1}) + K(\theta_i)}{2}, \qquad (6)$$

where A is the area of the grid mesh and dz_i is the distance between nodes $(i - 1)$ and i. To get this expression, we also approximate the values of K and D at the layers' interfaces by the arithmetic average of their values at the neighboring nodes.

[18] Equation (6), however, is not linear at first-order with respect to θ, because of the strong nonlinearity of $K(\theta)$ and $D(\theta)$ in Equations (3) and (4). To resolve this issue, we discretize the interval $[\theta_r; \theta_s]$ in 50 regular smaller subdomains where K and D are described by piecewise functions, respectively, linear in θ and constant. The appropriate piecewise functions are selected for each node depending on the value of θ_i at the beginning of each time step. Using these linearized K and D in equation (6), it becomes possible to construct a tridiagonal matrix system to solve $\theta_i(t + dt)$, at least for the inner nodes (i in $[2, N - 1]$).

[19] Additional information is required to solve θ_1 and θ_N. It consists of water fluxes Q_0 and Q_N at the top and bottom of the soil column, respectively. These fluxes need to be prescribed as boundary conditions at each time step and thus drive the evolution of the soil moisture profile. Q_0 is defined by the difference between infiltration into the soil and bare soil evaporation, and the bottom boundary condition is defined by free gravitational drainage:

$$Q_N = K(\theta_N). \qquad (7)$$

[20] *De Rosnay et al.* [2000] analyzed the influence of the vertical discretization on the simulated water and energy fluxes, to define the better compromise between precision and computation time. They eventually selected an 11-node configuration, with a geometric increase of the internode distance, and doubled between each consecutive couple of nodes. This kind of geometric configuration has the advantage of combining a high resolution near the surface to accurately simulate the partitioning between latent and sensible heat fluxes, and a lower resolution at the bottom to reduce computation times. It is thus used in most LSMs describing the vertical soil water fluxes based on the Richards equation. In ORCHIDEE, with 11 nodes in a 2 m soil column, we get thicknesses of 1 mm for the top layer, and 0.75 and 0.5 m for the tenth and eleventh layers, respectively (Figure 1).

2.4. New Bottom Boundary Conditions

[21] Equation (7) of free drainage implies that soil moisture θ is constant below the lower node, which is not always found in nature. In particular, when a shallow water table is present, we can get local increases of θ with depth because of capillary rise, or even saturation within the soil column. To describe such cases, we introduce the possibility of choosing between two new bottom boundary conditions.

[22] The first one is based on the free drainage calculation reduced by a coefficient F:

$$Q_N = F \cdot K(\theta_N), \qquad (8)$$

where $0 \leq F \leq 1$. This condition is equivalent to reducing the hydraulic conductivity K under the bottom of the soil column, which could be achieved alternatively by enhancing the exponential decay of K with depth. Setting $F = 0$ makes the bottom totally impermeable as in bucket-like models [*Manabe*, 1969], including the two-layer hydrology module of ORCHIDEE.

[23] The second new boundary condition is to impose saturation under the calculation node n_{sat} chosen by the user:

$$\theta_{i \geq n_{\mathrm{sat}}} = \theta_s. \qquad (9)$$

This implies the presence of a water table inside the modeled soil column. To do so, we first solve the diffusion equation over the 2 m soil column assuming that $F = 0$, then we adjust the resulting soil moisture to bring it back to saturation at nodes n_{sat} and below, if either upward diffusion or root absorption made it drop to unsaturated values. The required water flux is assumed to enter the soil column through the soil bottom interface, and thus represents negative drainage.

[24] The drainage reduction caused by these two new bottom boundary conditions leads to stronger hydraulic gradients at the bottom of the soil column. There, the coarse resolution related to the 11-node configuration is not sufficient anymore to simulate accurate water fluxes, and we had to increase the vertical discretization (Figure 1). To conserve model performances regarding surface fluxes partitioning, we kept the original discretization in the top 25 cm, with nine nodes. To increase resolution below, we opted for a regular discretization with an internode distance of about 15 cm, leading to increase the total number of nodes from 11 to 20. This allows us to more finely model the lower layers implicated in the drainage calculation, and it gives the possibility of prescribing a water table at a more finely defined depth.

[25] We eventually checked that, with this 20-node discretization, the numerical scheme described above was able to reproduce the analytical steady state solution of the original partial differential Richards equation without violating mass conservation for unsaturated soil profiles. As found by *Zeng and Decker* [2009] in the Community Land Model, our scheme cannot maintain perfectly saturated profiles, yet with a very small numerical error (less than 0.001% after 1 year).

3. Simulation and Evaluation Design

3.1. Coupling ORCHIDEE With an Atmospheric Model

[26] To study the influence of the soil bottom hydrology on the land surface fluxes and the atmosphere, we couple ORCHIDEE with LMDZ, the global atmospheric general circulation model of the Laboratoire de Météorologie Dynamique [*Hourdin et al.*, 2006], using the latest atmospheric physics package LMDZ5B [*Hourdin et al.*, 2012; *Rio et al.*, 2012]. LMDZ is used here with 39 atmospheric layers. This places the lowest level center at about 30 m above the surface. The horizontal grid mesh of LMDZ is rectangular and defines the one of ORCHIDEE over the land surface. Following *Coindreau et al.* [2007], we use 32 and 48 grid points in latitude and longitude, respectively, but the grid mesh is stretched to achieve a higher resolution, or zoom, over France, leading to a resolution of about 120 km in Western Europe (Figure 2), typical of current global models used for climate change studies.

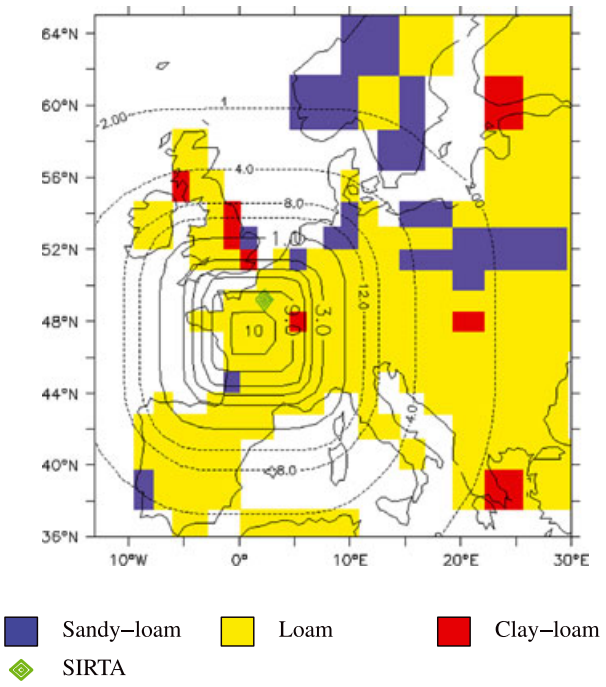

Figure 2. Nudging and soil texture over Europe. The SIRTA observatory appears as a green diamond. Contours show the nudging time constant, either in days (solid lines) or in hours (dotted line).

[27] The simulations analyzed in this paper cover the period 2000–2009, with prescribed interannually varying sea surface temperatures derived from observed monthly means. To give the coupled model LMDZ-ORCHIDEE independence from its initial conditions, the simulations are only analyzed over 2002–2009. In addition, to confront this coupled model to SIRTA's measurements (section 3.2), we use an atmospheric model configuration able to reproduce the observed regional weather. Following *Cheruy et al.* [2013], the simulations are forced to follow the real synoptic evolution by relaxing the simulated temperature and wind fields toward their values in the ERA-Interim reanalysis [*Dee et al.*, 2011] over 2000–2009. The nudging is strong if the relaxation of the model toward ERA-Interim is fast, as expressed by a small relaxation time constant. This time constant decreases when the grid cell size increases, to get a strong nudging outside from the zoomed area (time constant of 1 h). In contrast, LMDZ is almost free from nudging at the zoom center (time constant of 10 days), as well as all over France, where the time constant is longer than 1 day (Figure 2).

3.2. The SIRTA Observatory

[28] The above zoomed and nudged configuration of LMDZ-ORCHIDEE has been defined to facilitate the evaluation of this coupled model against measurements from the SIRTA observatory, located 20 km south of Paris, in France [*Haeffelin et al.*, 2005]. The grid cell it belongs to is very close to the zoom center (Figure 2), thus almost free from nudging. In our simulations, the SIRTA grid cell (approximately 120 × 120 km^2) is characterized by a medium-texture soil, and the main vegetation types are crops and grass (72%), bare soil (24%), and deciduous forest (4%), according to ORCHIDEE's forcing maps.

[29] The SIRTA was created by the IPSL at Palaiseau on the campus of the Ecole Polytechnique in 2000 and has since then been collecting many colocalized observations like atmospheric near-surface variables such as temperature, humidity, and precipitation but also sensible and latent heat fluxes derived from sonic anemometer measurements, radiative fluxes (Baseline Surface Radiation Network), and cloud/aerosol characteristics with in situ sensors, passive and active remote sensing instruments. The atmospheric observations used in this paper have been described in details by *Cheruy et al.* [2013], who showed they were representative of operational meteorological observations performed inside the SIRTA grid cell by Météo-France. *Cheruy et al.* [2013] used these observations to evaluate various physical parameterizations of LMDZ, with the exact same zoomed and nudged configuration as described above. They firstly showed that this configuration allows LMDZ to capture a large part of the interannual, seasonal, and synoptic variability observed at the SIRTA. Four different model versions were then tested, by combining two parameterizations of atmospheric physics (standard LMDZ5A versus new LMDZ5B, used in this paper) and two parameterizations of soil hydrology (2-layer bucket-type versus 11-layer Richards-based, used here). None of them, however, produced enough evaporation compared to SIRTA's observations, especially in summer when evaporation is maximum, which led to a systematic warm bias.

[30] To explore this issue, the present study benefits from additional measurements of soil moisture, at five depths down to 50 cm, using Theta-probes ML2X. The probes were calibrated in laboratory with respect to the volumetric weight of dry and saturated soil samples from the site. Porosity was estimated from the weight of saturated and totally desiccated soil samples. Based on five replicates for each soil depth, porosity equals 0.398 ± 0.024 m^3 m^{-3}. According to the USDA textural classification, the granulometric analysis defines a silt loam, consistent with the medium texture used in ORCHIDEE, but porosity, which defines the saturated water content θ_s, is slightly smaller according to the measurements than in ORCHIDEE (Table 1).

[31] The SIRTA is located on a plateau, the geology of which is typical of the central part of the Paris Basin and covers about two thirds of the SIRTA grid cell: it is made of tertiary sediments (with both aquifer and aquitard layers),

Table 2. Summary of the Performed Simulations

Name	Bottom Boundary Condition	Application Scale
REF	Free drainage (F = 1)	Globally
LF0.10	Drainage reduced by F = 0.10	SIRTA
LF0.01	Drainage reduced by F = 0.01	SIRTA
LF0.00	Impermeable bottom (F = 0)	SIRTA
LS2.0	Saturation imposed at 2.0 m	SIRTA
LS1.3	Saturation imposed under 1.3 m	SIRTA
LS0.5	Saturation imposed under 0.5 m	SIRTA
GF0.10	Drainage reduced by F = 0.10	Globally
GF0.01	Drainage reduced by F = 0.01	Globally
GF0.00	Impermeable bottom (F = 0)	Globally
GS2.0	Saturation imposed at 2.0 m	Globally
GS1.3	Saturation imposed under 1.3 m	Globally
GS0.5	Saturation imposed under 0.5 m	Globally

Table 3. Yearly and July-August (JA) Averages of Four Important Variables Observed at SIRTA[a]

Variable		W_{50} (mm)		LE (W m^{-2})		H (W m^{-2})		P (mm d^{-1})	
Measurement start		2007		2005		2006		2004	
Measurement coverage (%)		81.1		20.4		74.1		95.2	
Average period		Year	JA	Year	JA	Year	JA	Year	JA
SIRTA	with SIRTA filter	164.70	148.13	94.80	125.47	13.95	26.28	1.80	2.07
REF	with SIRTA filter	146.78	103.34	68.30	65.77	18.57	50.38	2.10	1.45
	Bias to SIRTA (%)	*–10.9*	*–30.2*	*–28.0*	*–47.6*	*+33.1*	*+91.7*	*+16.7*	*–30.0*
REF	in 2002–2009	153.28	150.77	53.50	75.61	20.37	55.62	2.16	1.44
	Effect of SIRTA filter (%)	*–4.2*	*–31.5*	*+27.7*	*–13.0*	*–8.8*	*–9.4*	*–2.8*	*+0.7*

[a]W_{50} is the total soil moisture in the top 50 cm, assuming linearity between two consecutive measurement or calculation nodes; LE is the latent heat flux; H is the sensible heat flux; P is the precipitation. The first two rows describe the quality of measurement sampling over time. The means of SIRTA measurements are compared to the reference simulation REF (see Table 2) using SIRTA filtering from measurement start to 2009, to define the bias of REF with respect to SIRTA observations. The last two rows give the mean values of REF in 2002–2009, to show the error caused by the SIRTA filter, relatively to the mean values in 2002–2009.

outcropping a Chalk aquifer formation, and overlaid by loess deposits. A detailed hydrogeological synthesis performed in the vicinity of the SIRTA revealed that the loess deposit lies on a rather continuous clay layer at a depth of 1 to 6 m [*Vernoux et al.*, 1999]. This results in a shallow water table, with no known piezometer, as it is disconnected from the main water table draining into the river network.

3.3. Performed Simulations

[32] The simulations presented in this paper, which all rely on the 20-node soil discretization, are summarized in Table 2. The REF simulation uses free drainage as a bottom boundary condition for soil water fluxes (equation (7)). We checked that it is very close to simulation NP-ORC11 in *Cheruy et al.* [2013], which uses the same parameterizations of atmospheric physics and soil hydrology, but with the original 11-node soil discretization. This confirms that the latter gives more accurate results with free drainage.

[33] To examine the influence of the two new boundary conditions introduced in section 2.4, we distinguish simulations with reduced drainage (equation (8)), using three different values of F from 0.1 to 0, and together referred to as simulations ⋆F⋆, from simulations with forced saturation (equation (9)), at three different depths between 0.5 to 2 m, and together referred to as simulations ⋆S⋆. To further analyze the role of these changes on the surface/atmosphere interactions, they are applied at two different scales, either locally (the bottom boundary condition is only changed over the SIRTA grid cell: simulations L⋆⋆) or globally (the changes are performed over all continental cells: simulations G⋆⋆).

4. Results

4.1. Biases of Simulations REF and L⋆⋆ at the SIRTA Observatory

[34] As most measurements, the SIRTA data exhibit interruptions, some of them being important as revealed in Table 3. To deal with this issue, we construct a filtered mean annual cycle for each observed variable, by considering separately each hourly time step of the year, which is assigned the average of the available data at this time step over the monitored years. This sequence of operations, hereafter called SIRTA filter, is different for each monitored variable, and applied to both the measurements and simulated variables for better comparison. The effect of these filters on the simulated averages is assessed in Table 3, by comparison to the means over the entire 2002–2009 period. This effect is negligible for sensible heat flux and precipitations, which are well monitored, but it decreases latent heat flux and soil moisture in summer because the available observations are sparse and mostly found when these variables are low.

[35] The biases of all the simulations with respect to SIRTA's observations are all analyzed after SIRTA filtering (Table 3, Figures 3, and 4). For the REF simulation, they are similar to the ones presented by *Cheruy et al.* [2013] for simulation NP-ORC11. They include an underestimation of the latent heat flux and an overestimation of the sensible heat flux. The simulated precipitation rates are not sufficient, especially in summer, which probably contributes to the turbulent fluxes biases.

[36] These biases are consistent with our soil moisture analysis, which shows that the simulated soil water contents are systematically underestimated at the three monitored depths (Figure 4). It also reveals that observed soil moisture at 50 cm is nearly constant and close to saturation (Figure 4c), as also evident from the observed soil moisture profiles (Figure 5b). In agreement with the local hydrogeology (section 3.2), this is suggestive of a shallow water table

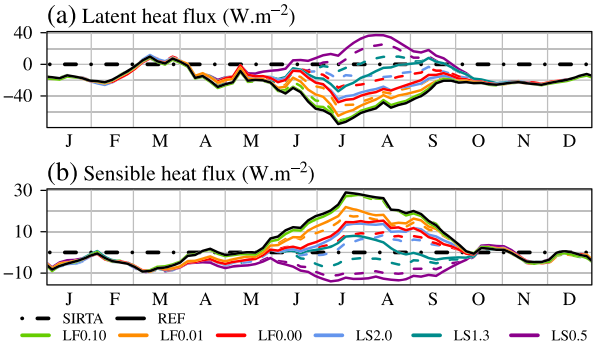

Figure 3. Monthly biases of simulated latent and sensible heat fluxes at the SIRTA, using SIRTA filtering, for simulations REF and L⋆⋆.

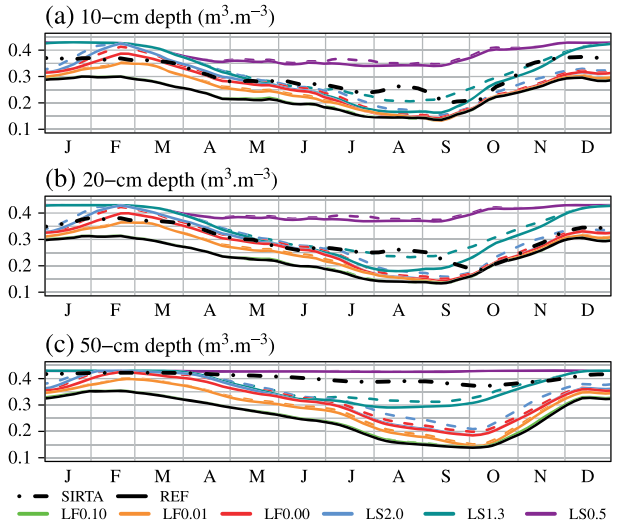

Figure 4. Soil moisture at 10, 20, and 50 cm at the SIRTA: mean annual cycles using SIRTA filtering, for observations and simulations REF and L⋆⋆.

at this depth, sustaining high soil moisture near the surface, especially in winter when the water table head is probably higher than 50 cm. The free drainage in the REF simulation prevents such saturation within the modeled soil column, and we further examine if the two new bottom boundary conditions proposed in section 2.4 can improve the soil moisture simulation and the related fluxes at the scale of the SIRTA grid cell (simulations L⋆⋆).

[37] Reducing the drainage by a factor F (simulations LF⋆) tends to increase soil moisture at the three depths, and this increase is logically all the stronger as F is close to 0. The first tenfold decrease of F, however, from REF to LF0.10, has a negligible effect, whether on soil moisture, surface fluxes, or near-surface meteorology (Table 4, Figures 3, and 4), which is consistent with the results from *Yeh and Eltahir* [2005]. The largest effect is obtained by prescribing an impermeable bottom ($F = 0$), but this modification is not sufficient to bring the simulated soil moisture up to the observed values, especially in summer.

[38] Imposing saturation within the soil has a stronger effect, with statistically significant changes of soil moisture and turbulent fluxes in all simulations LS⋆ compared to REF (Table 4). Simulation LS2.0, prescribing a water table

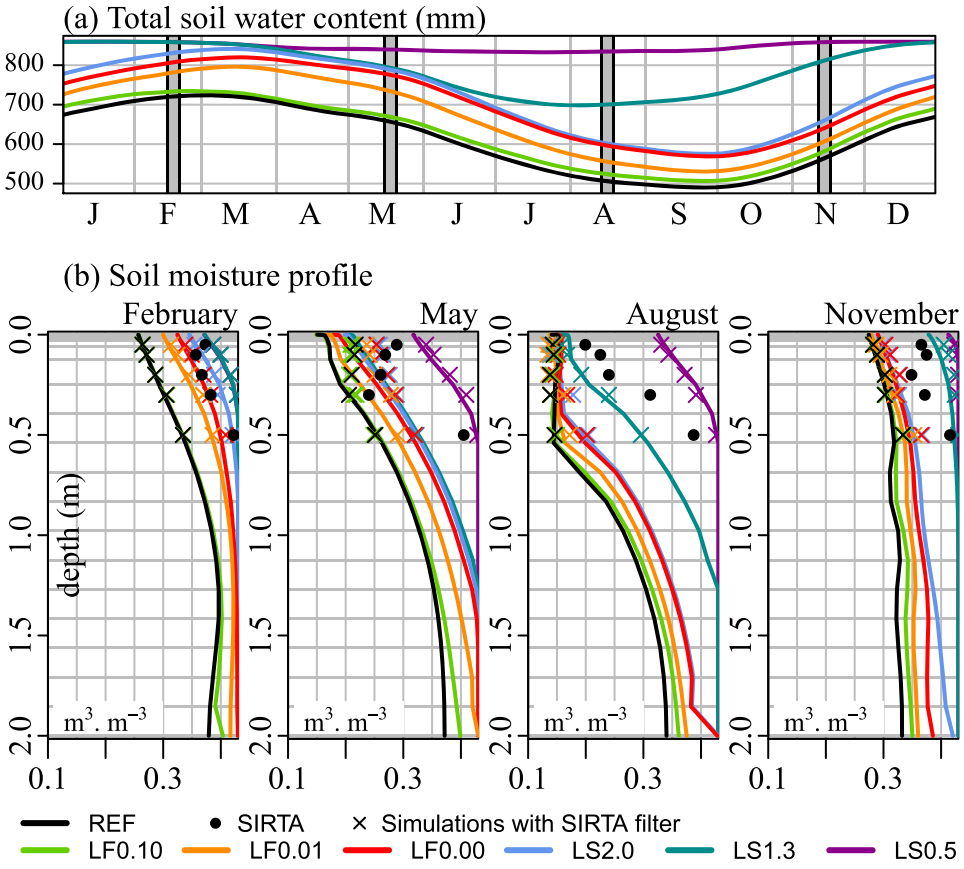

Figure 5. Soil moisture in the SIRTA grid cell for simulations REF and L⋆⋆: (a) mean annual cycle of total soil water content in 2002–2009 (without SIRTA filter, and with a 30 day running mean); (b) interannual mean vertical profiles of θ ($m^3\ m^{-3}$) over the four 5 day periods indicated by gray rectangles in Figure 5a; the bounds of θ in these four panels are the wilting point ($\theta_f = 0.10\ m^3\ m^{-3}$) and the saturation value ($\theta_s = 0.43\ m^3\ m^{-3}$). The black dots the measurement's mean over the four periods using SIRTA filter, and the colored crosses give the equivalent SIRTA filtered means for the different simulations.

Table 4. Differences in the SIRTA Grid Cell for the 12 Simulations With Modified Soil Bottom Boundary Condition With Respect to REF[a]

	W_{50} (mm)		LE (W m^{-2})		H (W m^{-2})		P (mm d^{-1})		T_a (K)		q_a (g kg^{-1})	
	Year	JA	Year	JA	Year	JA	Year	JA	Year	JA	Year	JA
LF0.10	1.12	3.55	0.27	1.13	–0.25	–0.99	0.00	0.00	–0.01	–0.02	0.01	0.02
LF0.01	**12.05**	**10.27**	2.53	8.77	–2.26	–7.44	–0.01	0.02	–0.01	–0.13	0.04	0.10
LF0.00	**18.78**	**15.73**	**4.43**	15.99	**–3.69**	–12.21	0.00	0.01	–0.03	–0.22	0.07	0.19
LS2.0	**23.12**	**16.82**	**5.02**	**17.87**	**–4.10**	**–13.75**	0.00	0.01	–0.03	–0.25	0.08	0.20
LS1.3	**45.15**	**59.04**	**7.71**	**27.81**	**–6.36**	**–21.55**	–0.01	0.00	–0.06	–0.38	0.13	0.34
LS0.5	**81.36**	**63.62**	**13.09**	**53.19**	**–10.81**	**–42.75**	0.00	0.02	–0.08	–0.64	**0.31**	**1.12**
GF0.10	**1.78**	**4.92**	0.61	2.49	–0.46	–1.83	0.02	0.01	–0.01	–0.05	0.02	0.04
GF0.01	**14.22**	**11.60**	**3.72**	14.11	**–3.05**	–11.51	0.08	0.21	–0.08	–0.43	0.13	0.41
GF0.00	**26.53**	**19.20**	**6.56**	**25.98**	**–5.33**	**–20.36**	0.14	0.52	–0.14	–0.69	0.21	**0.68**
GS2.0	**31.30**	**21.22**	**6.78**	**28.22**	**–5.97**	**–22.89**	0.16	0.66	–0.16	–0.89	**0.27**	**0.87**
GS1.3	**51.67**	**59.39**	**8.49**	**36.28**	**–7.82**	**–30.78**	0.27	0.92	–0.26	–1.30	**0.36**	**1.21**
GS0.5	**82.40**	**63.54**	**10.04**	**43.24**	**–9.88**	**–38.72**	0.35	**1.29**	–0.24	**–1.39**	**0.47**	**1.61**

[a]Yearly and July-August (JA) means over 2002–2009 (T_a and q_a are the lowest level air temperature and specific humidity, respectively; for other notations, see Table 3). Bold typing indicates statistically significant mean differences according to the Mann and Whitney test with a p value < 0.05.

at the bottom of soil column, is very similar to simulation LF0.00 with an impermeable bottom (Figures 3 and 4). The simulated soil moisture and turbulent fluxes get closer to SIRTA's observation when saturation is prescribed at 1.3 m, but prescribing saturation at 0.5 m leads to overestimated soil moisture and latent heat flux, and to underestimated sensible heat flux (Figure 3). This suggests that the water table could be found at the SIRTA between 0.5 and 1.3 m from the surface.

4.2. Sensitivity of Hydrological Processes to Local-Scale Changes

[39] To better apprehend the differences between simulations REF and L⋆⋆, the analysis is performed over 2002–2009 without SIRTA filtering. Total soil moisture in LS2.0, prescribing a water table at the bottom of the soil column, is close to total soil moisture in LF0.00 with an impermeable bottom (Figure 5a), as the latter exhibits a saturated 2 m node almost all the year long (Figure 5b). This is not the case in autumn (as illustrated by the November soil profile), and upward drainage is then momentarily required in LS2.0 to sustain saturation (Figure 6e). This difference at the soil bottom in autumn explains why soil moisture is higher in LS2.0 in winter (Figure 5b). Simulations LS1.3 and LS0.5 require a much larger upward drainage (Figure 6e) to force saturation at 1.3 and 0.5 m (Figure 5b), and the resulting soil moisture is higher over the entire soil column, and even too high in winter with respect to observations (Figure 4).

[40] The latent heat flux overestimation in LS0.5 seems mainly related to bare soil evaporation (Figure 6b), which is much higher in this simulation than in the others, with a delayed maximum, in summer instead of spring. The reason for this behavior is that the water table at 0.5 m allows surface soil moisture to remain high enough to hardly be limiting for bare soil evaporation. The decrease of this flux after June is then the result of energy limitation. In the other simulations (REF to LS1.3), bare soil evaporation starts to decrease earlier, in March, when transpiration starts to increase following vegetation growth (Figure 6a), which decreases soil moisture at the expense of bare soil evaporation. The LS0.5 transpiration (Figure 6a) also shows a delay of its maximum compared to the other L⋆⋆ simulations (Figure 6b), although to a lesser extent than for bare soil evaporation, but for the same reasons, since canceling water limitation allows the expression of energy limitation.

[41] The resulting increase in total evapotranspiration between simulations REF and L⋆⋆ does not significantly influence precipitation (Figure 6c and Table 4). Therefore, it decreases total runoff (not shown), which is weaker in simulations LS⋆ than LF⋆, and even becomes negative in simulation LS1.3 and LS0.5 in summer, by means

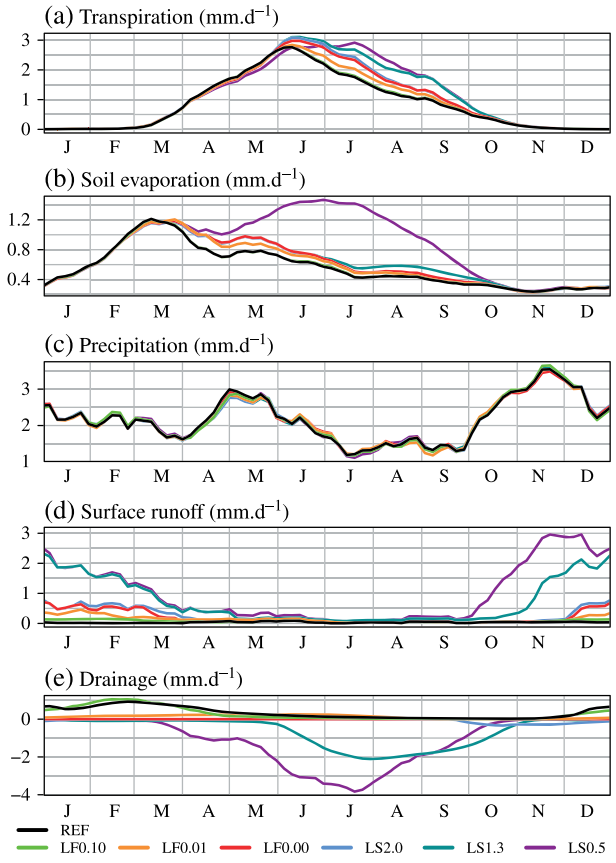

Figure 6. Water fluxes in the SIRTA grid cell for simulations REF and L⋆⋆: mean annual cycles in 2002–2009 (without SIRTA filter, and with a 30 day running mean).

of water conservation (with mean JA values of –1.8 and –3 mm d^{-1}, respectively). The overall decrease in total runoff results from opposite changes in surface runoff and drainage (Figures 6d and 6e). As already mentioned, the latter is directly decreased by the studied modifications of soil bottom hydrology. This happens in winter in all simulations L⋆⋆, and it also implies negative values in summer (upward flux) in simulations LS⋆. The resulting increase in soil moisture compared to REF (Figure 5a) reduces infiltration and in turn enhances surface runoff in winter (Figure 6d). The latter becomes very high in simulations LS1.3 and LS0.5 (which can reach 100% of the precipitation rate in winter), as a direct trade-off of imposed upward drainage.

4.3. Compared Impacts of Local and Global-Scale Changes at the SIRTA

[42] In all simulations L⋆⋆ and G⋆⋆, the studied changes in soil bottom drainage have an impact on the simulated climate in the SIRTA grid cell in summer period only.

[43] The increased latent heat flux leads to a cooling of both the surface (not shown) and the lower atmosphere (Figure 7d), with a more pronounced cooling in simulations G⋆⋆. This results in a decrease of the upward longwave (LW) flux from the surface, which increases net LW radiation to the land surface, to a larger extent in G⋆⋆ than in L⋆⋆ (Figure 7e). The shortwave (SW) radiation, in contrast, shows a very distinct response depending on the scale at which the soil bottom hydrology changes are considered. Albedo decreases with soil moisture in ORCHIDEE, so that the increase in soil moisture compared to REF (Table 4) contributes to increase net SW radiation in all simulations. In simulations G⋆⋆, however, the overall response of net SW radiation is a decrease (Figure 7f), which can be explained by the increase of cloudiness in these simulations (Figure 7c).

[44] Overall, the total net radiation increases in summer in all simulations L⋆⋆ and G⋆⋆ compared to REF (Figure 7g). This increase remains moderate but probably feeds back to increase the evaporation. In particular, the net radiation increase is maximum in LS0.5, which probably contributes to the fact that evaporation is lower in GS0.5 than in LS0.5, in combination with the higher atmospheric humidity moisture (Figure 7b) and lower surface temperature in G⋆⋆, which together decrease the water vapor deficit between the surface and the overlying atmosphere.

[45] Despite the clear increase of evaporation in the SIRTA grid cell, precipitation is not significantly sensitive to the local-scale modifications of drainage (in L⋆⋆), as shown in Table 4 and Figure 7c. This indicates that the additional evaporation resulting from drainage decreases in L⋆⋆ is not locally recycled into precipitation, even though it does increase atmospheric humidity (Figure 7b), in agreement with *Schär et al.* [1999]. The reason is that the SIRTA grid cell is subjected to atmospheric moisture divergence in summer, in the reference simulation REF (P-E = –1.15 mm d^{-1}), with further divergence in simulations L⋆⋆ with higher evaporation. In other words, because of advection, precipitation does not locally increase as much as evaporation.

[46] In contrast, the global-scale drainage reductions (simulations G⋆⋆) lead to increase precipitation rates compared to REF (leading to reduced net SW radiation as seen above). The SIRTA grid cell remains subjected to moisture

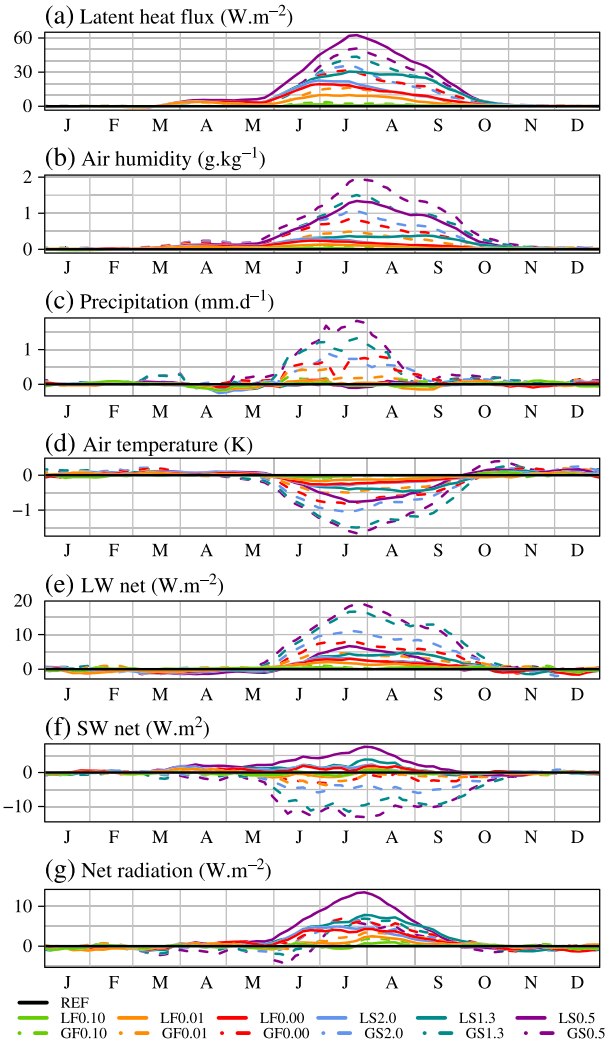

Figure 7. Differences in the SIRTA grid cell for simulations L⋆⋆ (plain lines) and G⋆⋆ (dashed lines) with respect to REF: mean annual cycles in 2002–2009 (without SIRTA filter, and with a 30 day running mean).

divergence in these simulations, but this divergence results in increasing atmospheric transport not only from the grid cell as in L⋆⋆, but also to the grid cell, which sustains higher precipitation rates. In other words, large-scale advection increases atmospheric humidity in simulations G⋆⋆ compared to L⋆⋆, and combined to lower atmospheric temperatures, it lowers the saturated specific humidity and facilitates condensation thus precipitation.

4.4. Water Cycle Sensitivity Over Europe

[47] According to the above analysis, the evaporation increase is not recycled into precipitation at the scale of one individual grid cell, but more regionally, as further explored below at the scale of Europe. There, as in the SIRTA grid cell, precipitation changes in simulations G⋆⋆ are restricted to summer, and related to both local characteristics and large-scale atmospheric transport. In the following, the regional-scale analysis is focused on two simulations, GF0.00 with an impermeable bottom in all land grid cells, and GS1.3 with a prescribed water table at 1.3 m in all land

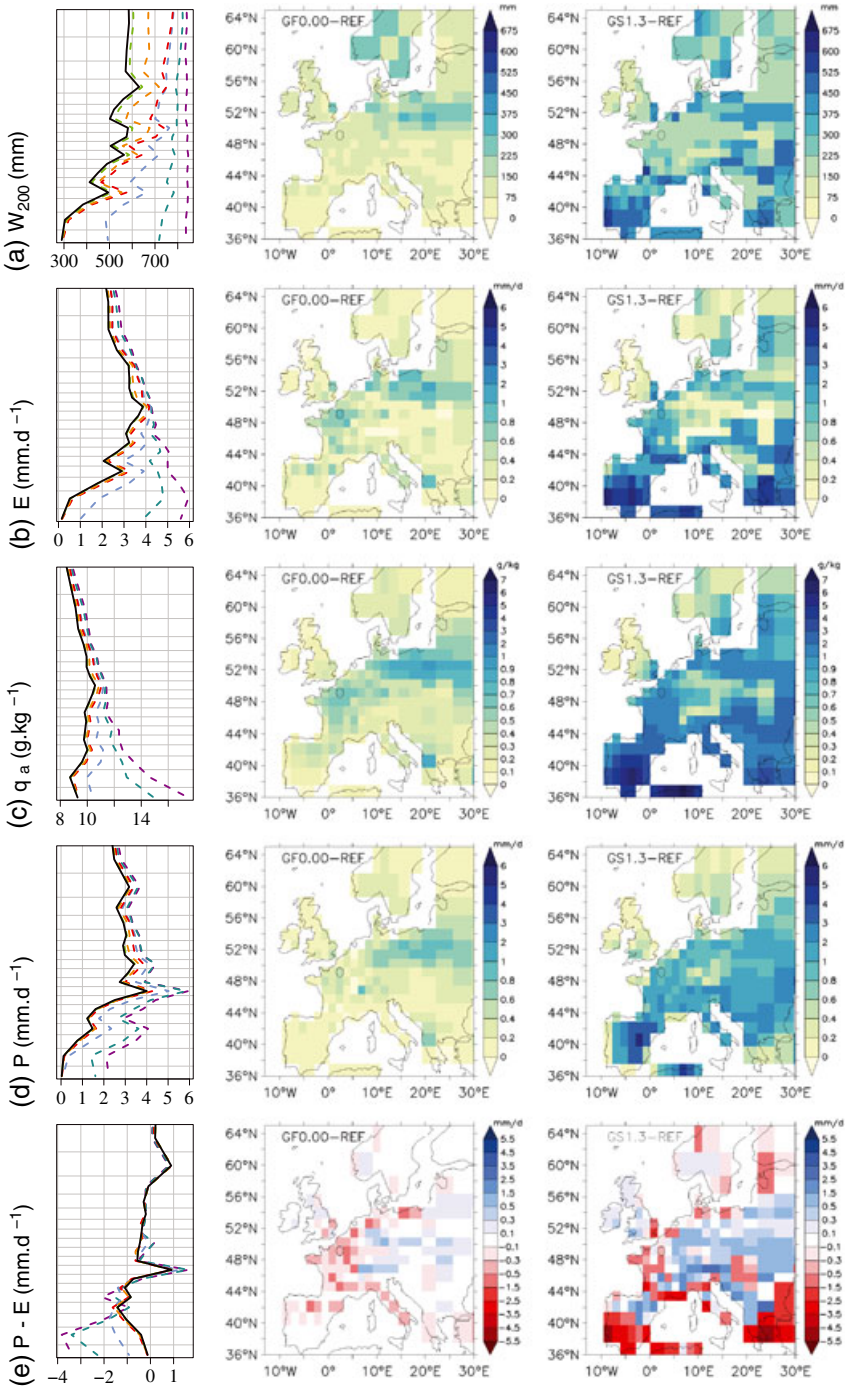

Figure 8. Geographic patterns of the sensitivity to soil bottom hydrological conditions in July-August (2002–2009 means) over the domain depicted in Table 2: (a) W_{200} is the total soil moisture in the 2 m soil column, (b) E is the evaporation rate, (c) q_a is the near-surface specific humidity, (d) P is the precipitation rate, and (e) P-E is the atmospheric moisture convergence; (left) zonal means of simulations REF and G⋆⋆, using the same color code as in Figure 7 (latitude varies between 36°N and 64°N on the y-axis, and the horizontal lines show the grid mesh meridian resolution), (center/right) differences between simulations GF0.00/GS1.3 and REF. The SIRTA observatory appears as a black circle.

grid cells. The results of the other simulations (REF and G⋆⋆) are summarized as zonal means (Figure 8).

[48] The patterns of soil moisture change compared to REF are different between GF⋆ and GS⋆ (Figure 8a). In the GF⋆ simulations, with reduced drainage, soil moisture mostly increases in areas where this variable is already high in REF, i.e., north of 40°N. Further south, precipitation is too small in summer to permit a significant increase of soil moisture by means of drainage reduction. In contrast, prescribing saturation in the soil column in GS⋆ necessarily increases soil moisture in these areas, and the increase compared to REF is much higher there than further north, where

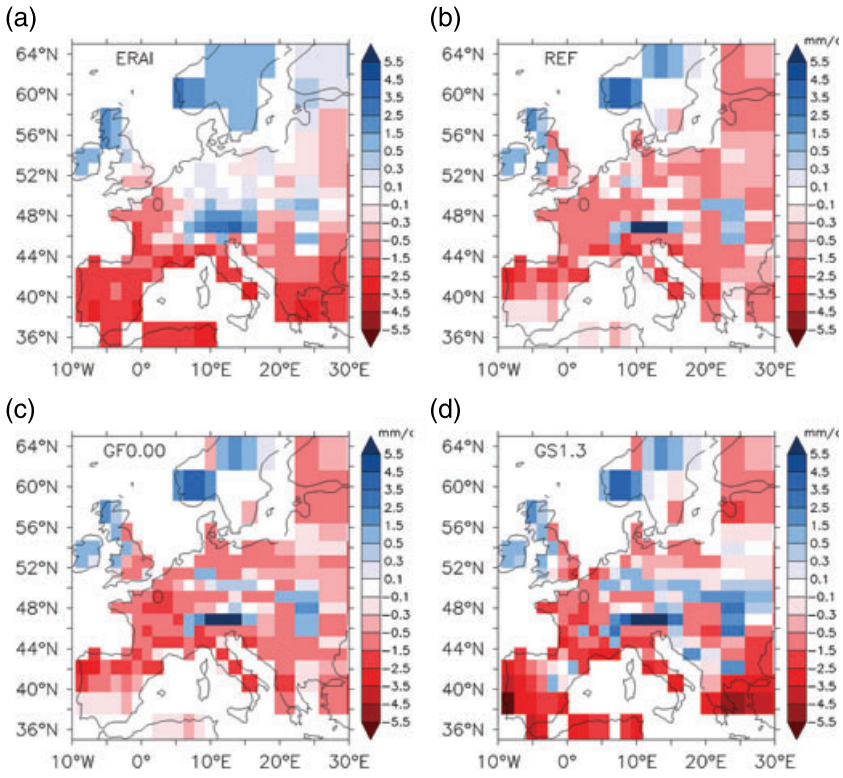

Figure 9. Geographic patterns of moisture convergence P-E over Europe in July-August (2002–2009 means, in mm d^{-1}): (a) ERA-I reanalysis, (b–d) simulations REF, GF0.00, GS1.3.

the moisture deficit with respect to full saturation is smaller in REF. In addition, in both simulations GF0.00 and GS1.3, the largest soil moisture increases appear over areas with sandy soils (Figure 2), in the Baltic peninsula, over North-Eastern Europe. The reason is that sandy soils have a much higher hydraulic conductivity than the other two soil classes (Table 1), so that their soil moisture is lower in REF (not shown), which allows a larger soil moisture increase.

[49] The evaporation increase patterns (Figure 8b) are very similar to the soil moisture increase patterns, which define areas where soil moisture limitation is reduced. The only exception is north of 55°N, where the strongest limiting factor to evaporation in REF is energy and not soil moisture. The precipitation increase (Figure 8d) is generally weaker in simulations GF⋆ than in GS⋆, where the atmosphere is moister (Figure 8c). In terms of patterns, precipitation increases over larger areas than evaporation in GS1.3, especially over Eastern Europe, while it is the opposite in GF0.00, where precipitation hardly changes in Western Europe. These differences between GF0.00 and GS1.3 are related to the distribution of atmospheric moisture sources over Europe, which is subjected to a mean eastward wind regime, in summer as all the year long. This results in a larger advection of atmospheric moisture over Western Europe, close to the Atlantic ocean source, than over Eastern Europe, which allows Western Europe to export more atmospheric moisture than Eastern Europe, as revealed by the largest moisture divergence over the former, both in REF and in the ERA-Interim reanalysis (Figures 9a and 9b).

[50] In this context, the increment of atmospheric moisture due to local evaporation increase in GF0.00 is relatively more important over Eastern than Western Europe, leading to higher precipitation increases over Eastern Europe. In GS1.3, in contrast, high precipitation increases are found everywhere south of 55°N. As explained above for the SIRTA grid cell, the increase of both advective and evaporative sources allows precipitation to increase in Western Europe despite enhanced moisture divergence, and the latter contributes to precipitation increase over Eastern Europe, where evaporation is weaker than over upstream Western Europe. As a result from these precipitation and evaporation changes, moisture divergence is enhanced over Western and Southern Europe (Figure 8e), where it is the highest in REF (Figure 9b), and it is reduced over Eastern Europe, where REF is only weakly divergent. These changes are more intense in GS1.3 and lead to moisture convergence in this simulation over Eastern Europe (Figure 9d). This explains why evaporation does not increase a lot in this area in GS1.3 compared to REF, probably by means of reduced humidity gradient (Figure 8c).

[51] These results are consistent with the zonal gradient in moisture recycling ratio found by *van der Ent et al.* [2010] over Europe, and with the "amplification mechanism" for soil-precipitation feedback suggested by *Schär et al.* [1999]. Note also that the striking similarity of the contrasted evaporation pattern in GS1.3 between Western and Eastern Europe with the results of *Lo and Famiglietti* [2011], with a water table coupled to the soil in a GCM.

4.5. Diurnal Cycle and Planetary Boundary Layer

[52] We also examined the mean diurnal cycle in summer for the energy fluxes and the near-surface meteorological variables (Figure 10). The results are perfectly consistent with what has been discussed above for the summer months,

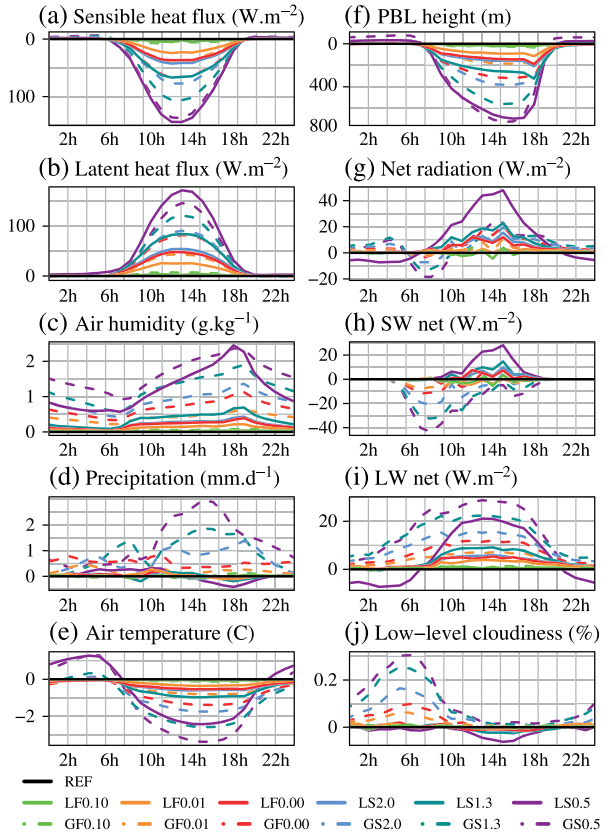

Figure 10. Mean diurnal cycles in July-August in the SIRTA grid cell: anomalies between simulations L⋆⋆ or G⋆⋆ on the one hand, and REF on the other hand (period 2002–2009 without SIRTA filter).

showing that the coupling between soil moisture and atmosphere takes place at the diurnal scale. In particular, the maximum sensitivity to the soil bottom hydrological conditions is usually found around noon, as the relaxation of soil moisture stress does not cancel energy limitation during the day. In contrast, the increase in precipitation, when present, i.e., in simulations G⋆⋆, is larger after noon. As detailed in *Cheruy et al.* [2013], this makes the diurnal cycle of summer precipitation closer to the observed one at the SIRTA site, and it comes from the new parameterization of atmospheric physics introduced in LMDZ, where deep convection triggering and intensity is controlled by subcloud processes [*Rio et al.*, 2009]. The planetary boundary layer (PBL) height is strongly affected as well (Figure 10f). The moister the soil is, the less the PBL develops, as a result of the different partitioning between sensible and latent heat fluxes. This is fully consistent with the results of *Schär et al.* [1999], who observed a 600 m lowering of the PBL height between their dry and wet experiments constructed to be representative of the interannual variability of summertime soil moisture. Finally, soil moistening leads to a slight increase of net radiation during daytime (Figure 10g), which is again consistent with the above monthly results and with *Schär et al.* [1999]. The partitioning between SW and LW radiation, however, depends on the spatial scale at which soil moisture is perturbed. For the global perturbations (simulations G⋆⋆), LW radiation is increased at night, as a result of a low-level cloudy layer which dissipates in the early morning (Figure 10j). According to *Cheruy et al.* [2013], this fog-like layer could be an artifact of a very moist surface layer coupled with an atmospheric vertical diffusion that is too weak.

4.6. Discussion of Global-Scale Impacts

[53] The above results have been obtained in a very particular framework, in which winds and temperatures are forced to follow the values of ERA-Interim outside from Europe, and are only free from this constraint over France (Figure 2). This strategy is very useful for process-oriented analyses in the free zone, as the simulations follow the observed synoptic variability, which allows a meaningful comparison to observations like the SIRTA ones [*Cheruy et al.*, 2013].

[54] Yet some important interactions are canceled at the regional to global scale. One of them is atmospheric cooling, which is mostly visible over France in our simulations, even in the most extreme cases, GS1.3 and GS0.5 (not shown). This prevents from quantifying the influence of the studied soil bottom boundary conditions on the dry/warm bias which is known to affect the IPSL climate model and many other [e.g., *Van Ulden and Van Oldenborgh*, 2006; *Klein et al.*, 2006; *Jacob et al.*, 2007]. Another canceled feedback is via large-scale circulation changes, since low-level winds are prescribed except over Western Europe. As a result, the changes in global-scale precipitation exhibited in simulations G⋆⋆ compared to REF (Table 5) mostly come from atmospheric moistening and ignored the effects of modified temperature and large-scale circulation patterns, although they are well-known controls of the precipitation patterns, especially in the Tropics [*Peixoto and Oort*, 1992; *Polcher*, 1995; *Ducharne and Laval*, 2000].

[55] Note that the total amount of water in the climate system is artificially increased in simulations ⋆S⋆ to sustain saturation at the prescribed depth. This explains the strong increases in both evaporation and precipitation in simulations GS⋆ compared to GF⋆ and REF, at the SIRTA and European scales (Table 4 and Figure 8). These increases become massive at the global scale (Table 5), when the artificial irrigation of tropical deserts is accounted for. Simulation GS0.5 can almost be seen as an aquaplanet simulation and was only designed as an extreme sensitivity experiment, with no expectation in terms of climate realism, except at the very local scale of the SIRTA, where soil moisture measurement reveal a permanent shallow water table.

[56] These limitations call for a revised analysis of the simulated climate sensitivity to the soil bottom hydrologic conditions, as developed in the next section.

5. Conclusions

[57] The mismatch between in situ data and modeled values at the grid cell scale is a well-known problem [e.g. *Chen*

Table 5. Global Land Averages in 2002–2009 and Comparison to the Observational Climatology of *Trenberth et al.* [2007], Which Covers 1979–2000

Variable	Unit	REF	GF0.00	GS1.3	GS0.5	Obs.
Precipitation	mm y^{-1}	719	734	978	1018	760
Evaporation	mm y^{-1}	516	538	912	980	491
Total runoff	mm y^{-1}	207	201	67	39	269

et al., 1997; *Running et al.*, 1999]. As a result, despite the probable representativity of both atmospheric and soil moisture measurements collected at the SIRTA with respect to the grid cell which contains it, we only used these data for a qualitative evaluation of the land-atmosphere modeling, which led us to thoroughly analyze the role of the hydrological boundary conditions at the bottom of the simulated soil column. Like *Decker and Zeng* [2009], we believe that it has been overlooked by land surface modelers, although very different approaches coexist, as noted in section 1.

[58] The first conclusion of our work regards the description of soil water flow in the ORCHIDEE LSM. Thanks to a refined vertical discretization, we were able to introduce new soil bottom boundary conditions, i.e., reduced drainage, and saturation within the soil column. This renders ORCHIDEE able to simulate a dynamic water table within the soil column, as realized in the SIRTA grid cell in simulation LF0.00. The resulting water table is intermittent (it vanishes in autumn) and too deep to sustain a sufficient evaporation in summer compared to SIRTA's observations. In line with *Gulden et al.* [2007] and *Guillod et al.* [2012], it would thus be interesting to check whether the simulated water table could be made perennial by modifications of the hydrodynamic properties of the soil column (Table 1).

[59] The second conclusion is that the tested hydrological bottom boundary conditions have an impact on soil moisture and land surface fluxes at both local and continental scales. Soil moisture logically increases when going from free drainage to impermeable bottom, then by prescribing saturation closer and closer to the surface, which requires upward drainage. The resulting increase in soil moisture is higher when/where the reference values are weak, i.e., in summer, in Southern Europe, and over sandy soils. Compared to SIRTA's measurements, we found that the best simulations in terms of land surface fluxes are the ones which describe the best soil moisture. This constitutes an interesting validation of (i) the evaporation processes in ORCHIDEE and (ii) the boundary layer processes in LMDZ, which benefits here from recent improvements regarding boundary layer physics, convection, and clouds [*Hourdin et al.*, 2012; *Rio et al.*, 2012].

[60] The simulation design applying the studied soil bottom boundary conditions changes at two scales, locally in simulations L⋆⋆ and globally in simulations G⋆⋆, has proven useful to separate their influence on soil hydrology and land surface fluxes, from the one on climate variables and the water cycle. Because of nudging, the latter could only be analyzed over Europe, and the analysis was restricted to summer, when soil moisture and evaporation are most sensitive to the studied changes. An important result is that local-scale changes of bottom boundary condition were not sufficient to influence precipitation in the SIRTA grid cell, despite significant changes in turbulent fluxes and atmospheric humidity.

[61] In contrast, the global-scale changes of bottom boundary condition were found effective in influencing the water cycle over Europe. We demonstrated a complex response of moisture convergence to the widespread land evaporation increase in simulations G⋆⋆, which can be related to differences in the relative weight of local *vs.* remote sources of moisture for precipitation between Western and Eastern Europe. This result is probably dependent on the boundary layer parameterizations [*Schär et al.*, 1999; *Cheruy et al.*, 2013], and in the present study, we found that the evaporation increase is not recycled into precipitation at the scale of one individual grid cell, but more regionally, as already shown by *Schär et al.* [1999] and *van der Ent et al.* [2010] for instance.

[62] The resulting increase of precipitation over Europe suggests that the warm/dry bias of many climate models in this region could be alleviated by including a sufficiently realistic water table description. Keeping in mind the limitations of our approach, discussed in section 4.6, this requires us to couple a freely evolving water table to an LSM, itself coupled to a freely evolving atmospheric model, as already achieved globally by *Lo and Famiglietti* [2011]. From there, an interesting sensitivity study would be to obtain dynamic water tables at different mean depths and to quantify their impact on surface fluxes and climate. Another perspective is to develop a realistic description of the water table, not only in terms of dynamics but also geographically, using the recently available global-scale hydrogeological data [*Dürr et al.*, 2005; *Strückmeier and Richts*, 2008; *Comunian and Renard*, 2009; *Gleeson et al.*, 2011b], as initiated by *Vergnes and Decharme* [2012]. In particular, the dependence of the climate sensitivity on the spatial scale at which the soil bottom boundary conditions are modified calls for a careful description of the "effective" area where the local water depth is shallow enough to increase soil moisture and evapotranspiration.

[63] **Acknowledgments.** This work received funding from the European Union, Seventh Framework Programme under grant agreements FP7/244067 (EUCLIPSE) and FP7/282672 (EMBRACE), and from the LABEX L-IPSL. Aurélien Campoy was supported by a grant from Région Ile-de-France. The simulations were performed using the IDRIS computational facilities (Institut du Développement et des Ressources en Informatique Scientifique, CNRS, France). The authors extend their acknowledgments to the staff of the SIRTA observatory, and to Pr. Yu-Jun Cui and Emmanuel De Laure from the Laboratoire Navier - CERMES (UMR 8205), for their help in soil sample characterization.

References

Abramopoulos, F., C. Rosenzweig, and B. Choudhury (1988), Improved ground hydrology calculations for global climate models (GCMs): Soil water movement and evapotranspiration, *J. Clim.*, *1*(9), 921–941.

Anyah, R., C. Weaver, G. Miguez-Macho, Y. Fan, and A. Robock (2008), Incorporating water table dynamics in climate modeling: 3. Simulated groundwater influence on coupled land-atmosphere variability, *J. Geophys. Res.*, *113*(D7), D07103, doi:10.1029/2007JD009087.

Betts, A. (2007), Coupling of water vapor convergence, clouds, precipitation, and land-surface processes, *J. Geophys. Res.*, *112*(D10), D10108, doi:10.1029/2006JD008191.

Beven, K., and M. Kirkby (1979), A physically based, variable contributing area model of basin hydrology, *Hydrol. Sci. J.*, *24*(1), 43–69.

Buckingham, E. (1907), *Studies on the Movement of Soil Moisture*, 61 p., US Government Printing Office, Washington.

Carsel, R., and R. Parrish (1988), Developing joint probability distributions of soil water retention characteristics, *Water Resour. Res.*, *24*(5), 755–769.

Chen, T. H., et al. (1997), Cabauw experimental results from the project for intercomparison of land-surface parameterization schemes, *J. Clim.*, *10*(6), 1194–1215.

Cheruy, F., A. Campoy, J. Dupond, A. Ducharne, F. Hourdin, M. Haeffelin, A. Chiriaco, and A. Idelkadi (2013), Combined influence of atmospheric physics and soil hydrology on the simulated meteorology at the SIRTA atmospheric observatory, *Clim. Dyn.*, *40*, 2251–2269.

Coindreau, O., F. Hourdin, M. Haeffelin, A. Mathieu, and C. Rio (2007), Assessment of physical parameterizations using a global climate model with stretchable grid and nudging, *Mon. Weather Rev.*, *135*(4), 1474–1489.

Comunian, A., and P. Renard (2009), Introducing wwhypda: A world-wide collaborative hydrogeological parameters database, *Hydrogeol. J.*, *17*(2), 481–489.

Darcy, H. (1856), *Les fontaines de la ville de Dijon*, Victor Dalmont, Paris.

De Rosnay, P., and J. Polcher (1998), Modelling root water uptake in a complex land surface scheme coupled to a GCM, *Hydrol. Earth Syst. Sci.*, *2*, 239–255.

De Rosnay, P., M. Bruen, and J. Polcher (2000), Sensitivity of surface fluxes to the number of layers in the soil model used in GCMs, *Geophys. Res. Lett.*, *27*(20), 3329–3332.

De Rosnay, P., J. Polcher, M. Bruen, and K. Laval (2002), Impact of a physically based soil water flow and soil-plant interaction representation for modeling large-scale land surface processes, *J. Geophys. Res*, *107*(D11), 4118.

Decharme, B., A. Boone, C. Delire, and J. Noilhan (2011), Local evaluation of the interaction between soil biosphere atmosphere soil multilayer diffusion scheme using four pedotransfer functions, *J. Geophys. Res.*, *116*(D20), D20126, doi:10.1029/2011JD016002.

Decker, M., and X. Zeng (2009), Impact of modified Richards equation on Global Soil moisture simulation in the Community Land Model (CLM3. 5), *J. Adv. Model. Earth Syst.*, *1*, 22 pp, doi:10.3894/JAMES.2009.1.5.

Dee, D., et al. (2011), The ERA-Interim reanalysis: Configuration and performance of the data assimilation system, *Q. J. R. Meteorolog. Soc.*, *137*(656), 553–597.

Dirmeyer, P., C. Schlosser, and K. Brubaker (2009), Precipitation, recycling, and land memory: An integrated analysis, *J. Hydrometeorol.*, *10*(1), 278–288.

D'Orgeval, T., J. Polcher, and P. De Rosnay (2008), Sensitivity of the West African hydrological cycle in ORCHIDEE to infiltration processes, *Hydrol. Earth Syst. Sci. Discuss*, *5*, 2251–2292.

Ducharne, A., and K. Laval (2000), Influence of the realistic description of soil water-holding capacity on the global water cycle in a GCM, *J. Clim.*, *13*, 4393–4413.

Ducharne, A., K. Laval, and J. Polcher (1998), Sensitivity of the hydrological cycle to the parametrization of soil hydrology in a GCM, *Clim. Dyn.*, *14*(5), 307–327.

Ducoudré, N., K. Laval, and A. Perrier (1993), Sechiba, a new set of parameterizations of the hydrologic exchanges at the land-atmosphere interface within the LMD atmospheric general circulation model, *J. Clim.*, *6*(2), 248–273.

Dürr, H., M. Meybeck, and S. Dürr (2005), Lithologic composition of the Earth's continental surfaces derived from a new digital map emphasizing riverine material transfer, *Global Biogeochem. Cycles*, *19*(4), GB4S10, doi:10.1029/2005GB002515.

Entekhabi, D., I. Rodriguez-Iturbe, and F. Castelli (1996), Mutual interaction of soil moisture state and atmospheric processes, *J. Hydrol.*, *184*(1), 3–17.

Famiglietti, J. S., and E. F. Wood (1994), Multiscale modeling of spatially variable water and energy balance processes, *Water Resour. Res.*, *30*, 3061–3078.

Gleeson, T., L. Marklund, L. Smith, and A. Manning (2011a), Classifying the water table at regional to continental scales, *Geophys. Res. Lett.*, *38*(5), L05401, doi:10.1029/2010GL046427.

Gleeson, T., L. Smith, N. Moosdorf, J. Hartmann, H. Dürr, A. Manning, L. van Beek, and A. Jellinek (2011b), Mapping permeability over the surface of the Earth, *Geophys. Res. Lett.*, *38*(2), L02401, doi:10.1029/2010GL045565.

Green, W., and G. Ampt (1911), Studies on soil physics, *J. Agric. Sci*, *4*(1), 1–24.

Guillod, B., E. Davin, C. Kündig, G. Smiatek, and S. Seneviratne (2012), Impact of soil map specifications for European climate simulations, *Clim. Dyn.*, 1–19.

Gulden, L., E. Rosero, Z. Yang, M. Rodell, C. Jackson, G. Niu, P. Yeh, and J. Famiglietti (2007), Improving land-surface model hydrology: Is an explicit aquifer model better than a deeper soil profile? *Geophys. Res. Lett.*, *34*(9), 9402, doi:10.1029/2007GL029804.

Haeffelin, M., et al. (2005), SIRTA, a ground-based atmospheric observatory for cloud and aerosol research, *Ann. Geophys.*, *23*, 253–275.

Hourdin, F., J.-Y. Grandpeix, C. Rio, and S. Bony (2012), *LMDZ5B: The Atmospheric Component of the IPSL Climate Model With Revisited Parameterizations for Clouds and Convection*, 2193–2222, vol. 40.

Hourdin, F., et al. (2006), The LMDZ4 general circulation model: Climate performance and sensitivity to parametrized physics with emphasis on tropical convection, *Clim. Dyn.*, *27*(7), 787–813.

Jacob, D., et al. (2007), An inter-comparison of regional climate models for Europe: Model performance in present-day climate, *Clim. Change*, *81*, 31–52.

Klein, S., X. Jiang, J. Boyle, S. Malyshev, and S. Xie (2006), Diagnosis of the summertime warm and dry bias over the U.S. Southern Great Plains in the GFDL climate model using a weather forecasting approach, *Geophys. Res. Lett.*, *33*(18), L18805, doi:10.1029/2006GL027567.

Kollet, S., and R. Maxwell (2008), Capturing the influence of groundwater dynamics on land surface processes using an integrated, distributed watershed model, *Water Resour. Res*, *44*(2), W02402.

Koster, R., and M. Suarez (2001), Soil moisture memory in climate models, *J. Hydrometeorol.*, *2*(6), 558–570.

Koster, R., M. Suarez, A. Ducharne, M. Stieglitz, and P. Kumar (2000), A catchment-based approach to modeling land surface processes in a general circulation model. 1. Model structure, *J. Geophys. Res.*, *105*(24), 809–24.

Koster, R., et al. (2004), Regions of strong coupling between soil moisture and precipitation, *Science*, *305*(5687), 1138–1140.

Krinner, G., N. Viovy, N. de Noblet-Ducoudré, J. Ogée, J. Polcher, P. Friedlingstein, P. Ciais, S. Sitch, and I. Prentice (2005), A dynamic global vegetation model for studies of the coupled atmosphere-biosphere system, *Global Biogeochem. Cycles*, *19*(1), 33, doi:10.1029/2003GB002199.

Liang, X., Z. Xie, and M. Huang (2003), A new parameterization for surface and groundwater interactions and its impact on water budgets with the variable infiltration capacity (VIC) land surface model, *J. Geophys. Res*, *108*(D16), 8613–8629.

Lo, M., and J. Famiglietti (2010), Effect of water table dynamics on land surface hydrologic memory, *J. Geophys. Res.*, *115*(D22), D22118, doi:10.1029/2010JD014191.

Lo, M., and J. Famiglietti (2011), Precipitation response to land subsurface hydrologic processes in atmospheric general circulation model simulations, *J. Geophys. Res.*, *116*(D5), D05107, doi:10.1029/2010JD015134.

Manabe, S. (1969), Climate and the ocean circulation 1. The atmospheric circulation and the hydrology of the Earth's surface, *Mon. Weather Rev.*, *97*(11), 739–774.

Maxwell, R., and N. Miller (2005), Development of a coupled land surface and groundwater model, *J. Hydrometeorol.*, *6*(3), 233–247.

Mualem, Y. (1976), A new model for predicting the hydraulic conductivity of unsaturated porous media, *Water Resour. Res.*, *12*(3), 513–522.

Niu, G., and Z. Yang (2003), The versatile integrator of surface atmospheric processes: Part 2: Evaluation of three topography-based runoff schemes, *Global Planet. Change*, *38*(1), 191–208.

Niu, G., Z. Yang, R. Dickinson, L. Gulden, and H. Su (2007), Development of a simple groundwater model for use in climate models and evaluation with Gravity Recovery and Climate Experiment data, *J. Geophys. Res*, *112*(D07), 103.

Oki, T., D. Entekhabi, and T. Harrold (2004), The global water cycle, in *State of the Planet: Frontiers and Challenges in Geophysics,* vol. 150, 414.

Peixoto, J., and A. Oort (1992), *Physics of Climate*, 520 pp., American Institute of Physics, New York.

Polcher, J. (1995), Sensitivity of tropical convection to land surface processes, *J. Atmos. Sci.*, *52*, 3143–3161.

Quesada, B., R. Vautard, P. Yiou, M. Hirschi, and S. Seneviratne (2012), Asymmetric European summer heat predictability from wet and dry southern winters and springs, *Nature Climate Change*, *2*, 736–741, doi:10.1038/nclimate1536.

Richards, L. (1931), Capillary conduction of liquids through porous mediums, *Physics*, *1*(5), 318–333.

Rio, C., F. Hourdin, J.-Y. Grandpeix, and J.-P. Lafore (2009), Shifting the diurnal cycle of parameterized deep convection over land, *Geophys. Res. Lett.*, *36*, 7, doi:10.1029/2008GL036779.

Rio, C., et al. (2012), Control of deep convection by sub-cloud lifting processes: The ALP closure in the LMDZ5B general circulation model, *Clim. Dyn.*, *40*, 2271-2292.

Running, S., D. Baldocchi, D. Turner, S. Gower, P. Bakwin, and K. Hibbard (1999), A global terrestrial monitoring network integrating tower fluxes, flask sampling, ecosystem modeling and EOS satellite data, *Remote Sens. Environ.*, *70*(1), 108–127.

Schär, C., D. Lüthi, U. Beyerle, and E. Heise (1999), The soil-precipitation feedback: A process study with a regional climate model, *J. Clim.*, *12*(3), 722–741.

Seneviratne, S., T. Corti, E. Davin, M. Hirschi, E. Jaeger, I. Lehner, B. Orlowsky, and A. Teuling (2010), Investigating soil moisture–climate interactions in a changing climate: A review, *Earth Sci. Rev.*, *99*(3), 125–161.

Stieglitz, M., M. Rind, J. Famiglietti, and C. Rosenzweig (1997), An efficient approach to modeling the topographic control of surface hydrology for regional and global modeling, *J. Clim.*, *10*, 118–137.

Strückmeier, W., and A. Richts (2008), Groundwater Resources Map of the World 1 : 25 000 000 (edition 2008), BGR and UNESCO. http://www.whymap.org/.

Trenberth, K., L. Smith, T. Qian, A. Dai, and J. Fasullo (2007), Estimates of the global water budget and its annual cycle using observational and model data, *J. Hydrometeorol.*, *8*(4), 758–769.

van der Ent, R., H. Savenije, B. Schaefli, and S. Steele-Dunne (2010), Origin and fate of atmospheric moisture over continents, *Water Resour. Res.*, *46*(9), W09525, doi:10.1029/2010WR009127.

Van Genuchten, M. (1980), A closed-form equation for predicting the hydraulic conductivity of unsaturated soils, *Soil Sci. Soc. Am. J.*, *44*(5), 892–898.

Van Ulden, A., and G. Van Oldenborgh (2006), Large-scale atmospheric circulation biases and changes in global climate model simulations and their importance for climate change in Central Europe, *Atmos. Chem. Phys.*, *6*(4), 863–881.

Varado, N., I. Braud, P. Ross, and R. Haverkamp (2006), Assessment of an efficient numerical solution of the 1-D Richards' equation on bare soil, *J. Hydrol.*, *323*(1), 244–257.

Verant, S., K. Laval, J. Polcher, and M. De Castro (2004), Sensitivity of the continental hydrological cycle to the spatial resolution over the Iberian Peninsula, *J. Hydrometeorol.*, *5*(2), 267–285.

Vergnes, J.-P., and B. Decharme (2012), A simple groundwater scheme in the TRIP river routing model: Global off-line evaluation against GRACE terrestrial water storage estimates and observed river discharges, *Hydrol. Earth Syst. Sci.*, *16*(10), 3889–3908, doi:10.5194/hess-16-3889-2012.

Vernoux, J.-F., J. Barbier, M. Donsimoni, J.-J. Seguin, and J. Vairon, (1999), Etude hydrogeologique du plateau de Saclay (Essone), *Tech. rep.*, 77 p, 30 figures, 10 tableaux, 3 annexes., Bureau de Recherches Géologiques Miniéres, rapport BRGM SGR/IDF R 40840.

Yeh, P., and E. Eltahir (2005), Representation of water table dynamics in a land surface scheme. Part I: Model development, *J. Clim.*, *18*(12), 1861–1880.

York, J., M. Person, W. Gutowski, and T. Winter (2002), Putting aquifers into atmospheric simulation models: An example from the Mill Creek Watershed, northeastern Kansas, *Adv. Water Resour.*, *25*(2), 221–238.

Zeng, X., and M. Decker (2009), Improving the numerical solution of soil moisture-based Richards equation for land models with a deep or shallow water table, *J. Hydrometeorol*, *10*(1), 308–319.

Zobler, L. (1986), *A World Soil Profile for Global Climate Modelling*, 87802, NASA Technical Memorandum.